Cosmology with Equivalence Principle Breaking in the Dark Sector

Jose Ariel Keselman*

Physics department, Technion, Haifa 32000, Israel

Adi Nusser

Physics Department and the Asher Space Research Institute, Technion, Haifa 32000, Israel

P. J. E. Peebles

Joseph Henry Laboratories, Princeton University, Princeton, NJ 08544, USA

A long-range force acting only between nonbaryonic particles would be associated with a large violation of the weak equivalence principle. We explore cosmological consequences of this idea, which we label ReBEL (daRk Breaking Equivalence principLe). A high resolution hydrodynamical simulation of the distributions of baryons and dark matter confirms our previous findings that a ReBEL force of comparable strength to gravity on comoving scales of about $1\,h^{-1}$Mpc causes voids between the concentrations of large galaxies to be more nearly empty, suppresses accretion of intergalactic matter onto galaxies at low redshift, and produces an early generation of dense dark matter halos. A preliminary analysis indicates the ReBEL scenario is consistent with the one-dimensional power spectrum of the Lyman-Alpha forest and the three-dimensional galaxy auto-correlation function. Segregation of baryons and DM in galaxies and systems of galaxies is a strong prediction of ReBEL. ReBEL naturally correlates the baryon mass fraction in groups and clusters of galaxies with the system mass, in agreement with recent measurements.

I. INTRODUCTION

The ΛCDM cosmology (the relativistic hot Friedmann-Lemaître model with a cosmological constant and Cold Dark Matter, DM) is very successful at matching the large-scale distributions of matter and radiation, including the angular Power Spectrum (PS) and polarization of the cosmic microwave background and the galaxy correlation functions and PS, if one allows for mild biasing between the mass and galaxy distributions. But there are problems with structure formation, and there is a possible remedy, ReBEL, a long-range force of attraction operating only on the DM. This has been studied in numerical simulations of structure formation in [1–4]. Here we present new results on structure formation on cosmological length scales from joint modeling of baryons and DM using the Smoothed-Particle Hydrodynamics (SPH) method and the DM TreePM code Gadget2 [5], modified to take account of the added force on the DM. Our two simulations compare evolution of structure with and without ReBEL. We also use the Halo Occupation Distribution (HOD) framework to compare model predictions to statistical measures of large-scale structure derived from recent galaxy surveys.

We consider ReBEL in the form of an attractive force between DM particles alone of the form

$$\mathbf{F} = -\frac{\beta G m^2}{a^2 r^2} e^{-r/r_{\mathrm{s}}} \left(\frac{1}{r} + \frac{1}{r_{\mathrm{s}}} \right) \mathbf{r}, \tag{1}$$

as in [1, 4, 6]. Here $a\mathbf{r}$ is the physical separation vector, where $a(t)$ is the cosmological expansion parameter. The screening length, here set to $r_{\mathrm{s}} = 1\,h^{-1}$Mpc (where the Hubble parameter is $H_0 = 100h\,\mathrm{km\,s^{-1}\,Mpc^{-1}}$), is constant in comoving coordinates. The Newtonian gravitational constant is G and the DM particle mass is m.

Frieman and Gradwohl pointed out the constant β that measures the strength of the ReBEL force is bounded above by its tendency to separate stars from DM [7], contrary to the observation that some dwarf spheroidal companions of the Milky Way have retained their DM halos. Kesden & Kamionkowsky [2] made the excellent point that a moderately strong ReBEL, with $\beta \sim 0.1$, separates stars from DM in a satellite galaxy in one-sided stream. This is quite contrary to the observed classical double stream of stars in the Sagittarius galaxy [8]. We consider here the stronger ReBEL force $\beta = 1$. This passes the Frieman-Gradwohl test in the cases considered in [4]. It also passes the Kesden-Kamionkowsky test because ReBEL would pull the Sagittarius stars away from the DM halo before close passages by the Milky Way tidally disrupt the DM-free but still gravitationally bound star cluster in the observed two streams. The process is illustrated in Figures 3 and 11 in Keselman et. al. [4]. Bean et al. [9] show that $\beta \simeq 1$ also so far passes the constraints from the cosmological tests.

Section II reviews issues that motivate analysis of observational consequences of ReBEL, with a guide to the issues studied in the present paper. The numerical modelling is described in § III. Results are presented in § IV, beginning with a general description of the main results. The more elaborate analyses are divided into several subsections describing the different algorithms used for find-

*Electronic address: kari@tx.technion.ac.il

ing halos and voids and the method used to calculate the Lyα PS. A concluding discussion is presented in § V.

II. ISSUES AND MOTIVATIONS

We review here our selection of apparent challenges to structure formation that motivate consideration of the addition of ReBEL to ΛCDM. For another overview of the situation see [10].

The ΛCDM cosmology tends to over-populate halos of galaxies with satellites and voids with dwarf galaxies. The former [11–15] may be resolved by the effect of plasma pressure or winds that leave low mass DM halos with too few baryons to be observable. ReBEL offers another stripping effect, the differential acceleration of baryons and DM [4], and ReBEL may also promote more complete merging of small halos [1, 3]. The latter issue [16–18] is best expressed as a comparison of counts of galaxies actually observed in denser regions to what is seen in voids [19, 20]. In particular, the nearby Local Void contains just two known galaxies [21–23], while scaling from counts of galaxies observed elsewhere would predict the presence of about 15 to 30 galaxies with $-18 \lesssim M_{\mathrm{B}} \lesssim -10$ in the Local Void. The possible role of a ReBEL force in more completely emptying voids is explored in [4] and in § IV C.

While ΛCDM correctly predicts the general density profile of clusters of galaxies it tends to underestimate the concentration parameter, resulting in profiles that are too shallow with respect to observations based on strong and weak lensing [24, 24–26] and X-Ray emission [27]. We show in § IV B 3 that ReBEL increases the concentration by earlier assembly of clusters, which is in the direction indicated by the observations.

The ΛCDM cosmology underpredicts the abundance of disk-dominated galaxies [28, 29]. This is because merging accretion of extragalactic debris by DM halos of mass $10^{11} - 10^{13} M_{\odot}$ is predicted to continue to modest redshifts, causing thin disks that formed earlier to thicken into bulges by gravitational heating [30–33]. The predicted merging also is difficult to reconcile with the insensitivity to environment of the correlations among luminosity, radius, velocity dispersion and color in early-type and late-type galaxies [34–37]. We show in § IV B 2 that ReBEL promotes significantly earlier assembly of galaxies, which is in the direction wanted to relieve these problems.

The earlier structure formation under ReBEL would promote earlier reionization. Polarization measurements of the cosmic microwave background radiation indicate reionization of hydrogen by redshift 11, implying early structure formation [38, 39]. Galaxy/star formation in the ΛCDM with $\sigma_8 \approx 0.9$ could be early enough to account for such early reionization. However, extreme efficiency of UV photon production by early structures is needed for $\sigma_8 \approx 0.8$, the value favored by WMAP data [40]. ReBEL may relieve this condition.

Earlier merging would lead to stronger clustering of more massive galaxies now and the clustering of the intergalactic medium at redshift $z \sim 3$ observed as the Lyman-Alpha forest. The galaxy two-point correlation function and PS found in [3] in and here in § IV A 3 seem to be consistent with what is observed within the usual uncertainties of biasing. Dark matter halos are more massive in ReBEL (§ IV B 1), and the difference from the standard model is more pronounced at redshift $z = 1$ than the present. Remaining to be explored is the effect on the galaxy luminosity function. We conclude in § IV A 2 that the model parameters for the intergalactic medium at $z \sim 3$ can be adjusted within the available constraints to fit the one-dimensional Lyα PS about equally well in the standard model and in ReBEL with $\beta = 1$.

Groups of galaxies in which the virial temperature is large enough that intragroup plasma would be expected to be detectable in X-ray emission are observed to contain a significantly smaller baryon mass fractions than the cosmic mean (e.g. [41–45]). This may be a result of the tendency of ReBEL to segregate DM from baryonic matter, as shown in [46, 47] and further analyzed in § IV B 4.

The more rapid structure formation that seems to be indicated by the phenomenology we have reviewed could follow from at least three adjustments of ΛCDM: a departure from near scale-invariant adiabatic Gaussian initial conditions, a modified gravity with a departure of the inverse square law that preserves the weak equivalence principle [48], or, in general relativity theory, a long-range force that operates only on the DM particles. We consider this last option. Superstrings offer scenarios for such a force in the dark sector [49–51]. The force would cause the accelerations of cosmic objects to depend on their relative DM content, in what may be termed a breaking of the weak equivalence principle, or ReBEL (daRk Breaking Equivalence principLe). Bovy and Farrar [52] point out that if the DM interacted with visible matter strongly enough to allow laboratory DM detection then ReBEL could induced a fifth force in the visible sector that is much stronger than allowed by the Eötvös laboratory constraint. It should be noted, however, that a laboratory DM detection need not vitiate ReBEL, for there may be several types of DM in addition to massive neutrinos, including one with a significant interaction with the visible sector but not ReBEL , and another that is coupled to ReBEL but not the visible sector [52–54].

III. NUMERICAL MODELLING

A. The simulations

We have modified the Gadget2 code to include, in addition to gravity, the force in Eq. 1 operating between the DM particles only. The simulations include
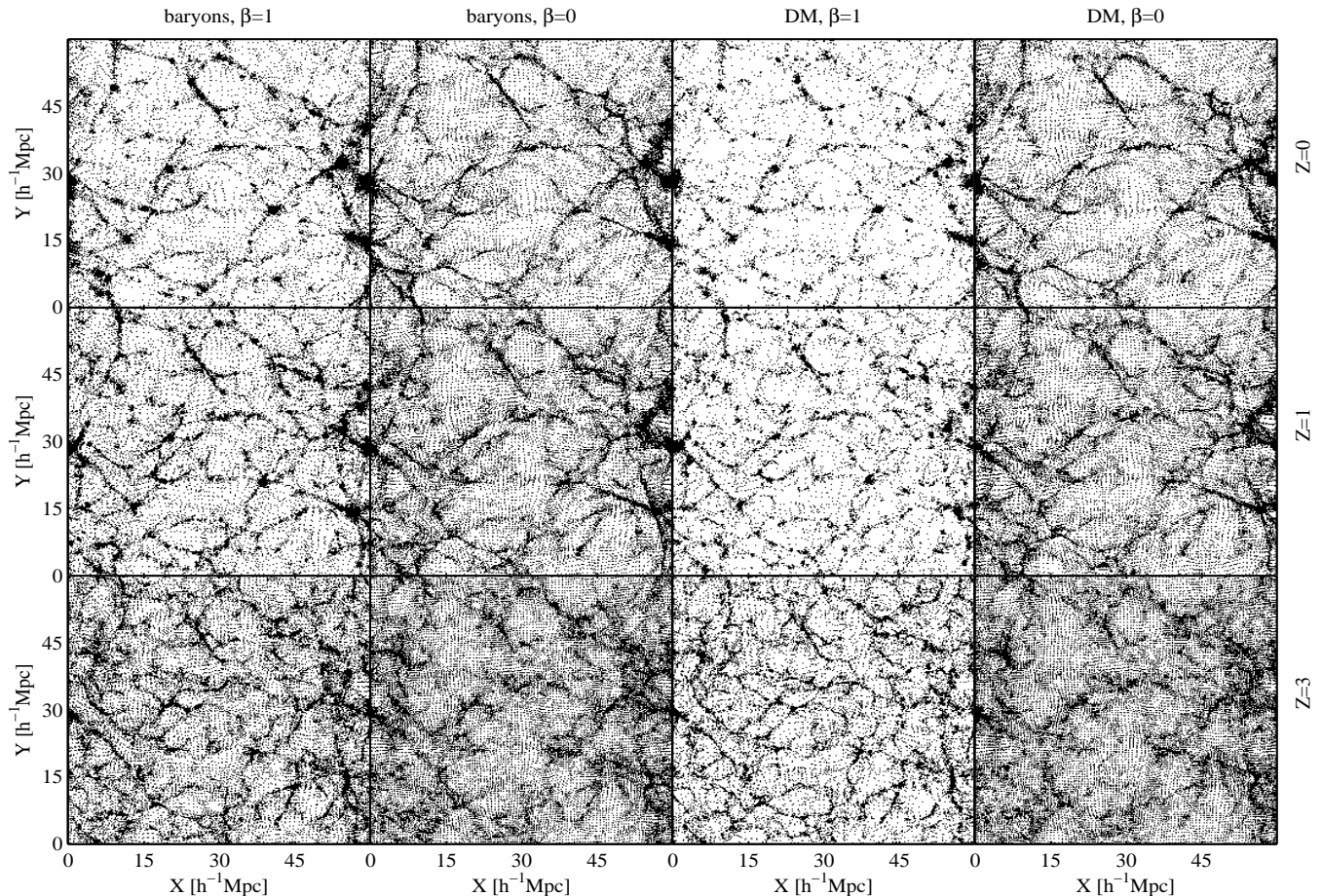
FIG. 1: Particle distributions in a slice $2\,h^{-1}$Mpc thick. Only a random subsample, containing 10% of the particles is shown.

gas (baryonic) particles subject to pressure and gravitational forces but not the ReBEL force. The hydrodynamic equations are solved using the particle-based SPH method in Gadget2. The modification is such that the error in the calculation of the total force is the same as in the standard, public Gadget2. Appendix A describes the details of the modification. The modified code is tested as described in appendix B.

We obtain for comparison two simulations, with and without ReBEL. The cosmological background is the same in the two simulations, with density parameters $\Omega_{DM} = 0.23$, $\Omega_{BAR} = 0.046$, $\Omega_\Lambda = 0.72$, with Hubble parameter $h = 0.7$, all consistent with [55]. Encouraged by our previous results [1, 4] we adopt the screening length $r_s = 1\,h^{-1}$Mpc and ReBEL force parameter $\beta = 1$ in Eq. 1.

The simulation box is $60\,h^{-1}$Mpc on the side. It contains 128^3 DM particles and an equal number of baryonic particles. The DM particles have mass $6.57 \times 10^9\,h^{-1}M_\odot$, the baryon particles $1.31 \times 10^9\,h^{-1}M_\odot$. The bayonic equation of state is that of a perfect gas with $\gamma = 5/3$, neglecting energy sinks and sources. The specific entropy is conserved except at shocks. The initial entropy corre-

sponds to a temperature of $5\,$K at the starting redshift of the simulation, $z = 1000$. Shock waves generated in collapsing structures heats the gas to the much higher temperatures noted in the next section.

Our two simulations start from identical initial conditions at $z = 1000$, when the ReBEL force is assumed to start operating [51]. The initial conditions are generated from the linear PS of the standard ΛCDM [56] cosmology for our choice of parameters. We use the Zel'dovich displacements of points and their peculiar velocities in an initially uniform body-centered cubic lattice. The initial density fluctuations are normalized so the linearly extrapolated (without ReBEL) rms value of the density fluctuations at $z = 0$ in spheres of radius $8\,h^{-1}$Mpc is $\sigma_8 = 0.8$.

To identify DM halos in the simulation we apply the "Friends-of-Friends" (FOF) algorithm [57]. The inter-particle linking length is $b = 0.2$ in units of the mean particle separation.

B. Galaxies and Halos in the simulations

To compare results from the simulations to the observed large-scale distribution of galaxies we need a recipe for identifying mock galaxies. The most thorough way is to trace halos in the simulation forward in time and assign them galaxies according to semi-analytic galaxy formation recipes (e.g. [58]), but this requires simulations with larger resolution than presented here. We use instead the simpler Halo Occupation Distribution (HOD) framework [59], in which a DM halo with mass M_h above a threshold M_{min} contains a central galaxy, and, above a larger threshold M_1, satellite galaxies.

We adopt HOD parameters such that galaxies in the simulations represent the observed galaxies more luminous than $L_\star/2.5$, corresponding to absolute magnitude $M_r = -19.5$, with the observed number density $0.01\,h^3\,\mathrm{Mpc}^{-3}$ adopted from table 2 in [60]. In the conventional case, $\beta = 0$, the HOD parameters also produce a satisfactory fit to the observed number density of voids above a mass threshold of $10^{10}\,h^{-1}\mathrm{M}_\odot$ and the distributions of galaxies within them [20]. The $\beta = 1$ case requires a modification of the HOD prescription to fit the voids, as we will describe.

In the $\beta = 0$ case the number of satellite galaxies assigned to a halo of mass M_h is drawn from a Poison distribution with mean

$$\langle N \rangle = \left(\frac{M_h}{M_1} \right)^\alpha . \qquad (2)$$

The three parameters M_{min}, M_1, and α are fixed to match the galaxy number density and correlation function. Each satellite is placed on a randomly chosen halo DM particle.

To match both the the properties of voids and the distribution of bright galaxies in the $\beta = 1$ case we must modify the HOD prescription. We adopt a broken power-law model for the number of satellites in a halo,

$$\langle N \rangle = \begin{cases} \left(\frac{M_h}{M_1} \right)^\gamma & \text{if } M_h < M_s, \\ \left(\frac{M_s}{M_1} \right)^\gamma + \left(\frac{M_h - M_s}{M_1} \right)^\alpha & \text{otherwise,} \end{cases} \qquad (3)$$

which is continuous at the mass scale M_s. Also, we need a more extended distribution of satellite galaxies than results from the $\beta = 0$ prescription. We achieve this by increasing the satellite distances from the halo center by a constant multiplicative factor, ζ, relative to the DM distribution in the host halo. This produces a satellite distribution similar to that of the $\beta = 0$ case [61, 62].

IV. RESULTS

Fig. 1 shows a representative distribution of the gas and DM particles in a slice $2\,h^{-1}\mathrm{Mpc}$ thick through the simulations at three redshifts, as indicated in the figure. Comparison between the DM distributions (two columns

to the right) with ReBEL ($\beta = 1$) and the standard model ($\beta = 0$) clearly shows the ReBEL enhancement of small-scale clustering of the DM: voids are emptier and the presence of individual clumps more pronounced. There also is a stronger redshift evolution in the DM particle distribution for $\beta = 1$. (Here and throughout we use coordinates comoving with the general expansion.) In the $\beta = 0$ simulation the baryonic component closely follows the DM on scales larger than the Jeans length, as expected. Also as expected is the behavior for $\beta = 1$, where the baryons are affected by the ReBEL force only indirectly, through the gravitational attraction of the more strongly clustered DM. The differences between the baryon distributions in the $\beta = 1$ and $\beta = 0$ simulations in the two columns to the left, though important, are indeed less pronounced than in the DM distributions.
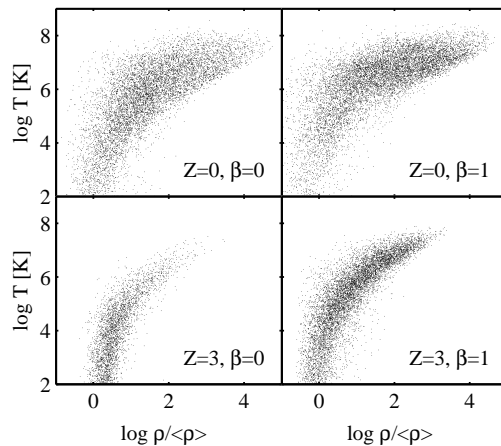

FIG. 2: Scatter plot of temperature versus density of particles in the $\beta = 0$ (left panels) and $\beta = 1$ (right) simulations, at redshifts $z = 0$ (top panels) and $z = 3$ (bottom)

Fig. 2 shows a scatter plot of temperatures and overdensities of 10^4 SPH gas particles in the two simulations at two redshifts. The top-right corner of this $T - \rho$ plane is more densely populated for $\beta = 1$, and the difference is more pronounced at $z = 3$: in ReBEL more baryons are in dense hot regions. Apart from that the diagrams for ΛCDM and ReBEL are similar, consistent with the rough similarity of the baryon distributions in Fig. 1.

A. Correlation Functions and Power Spectra

1. The distributions of baryons and dark matter

The clustering properties of the particle distributions measured by their PS are shown in in Fig. 3 at several redshifts. Thin lines correspond to the standard scenario, $\beta = 0$, while the thick lines show the effect of ReBEL with $\beta = 1$. As expected, the PS in the two simulations are
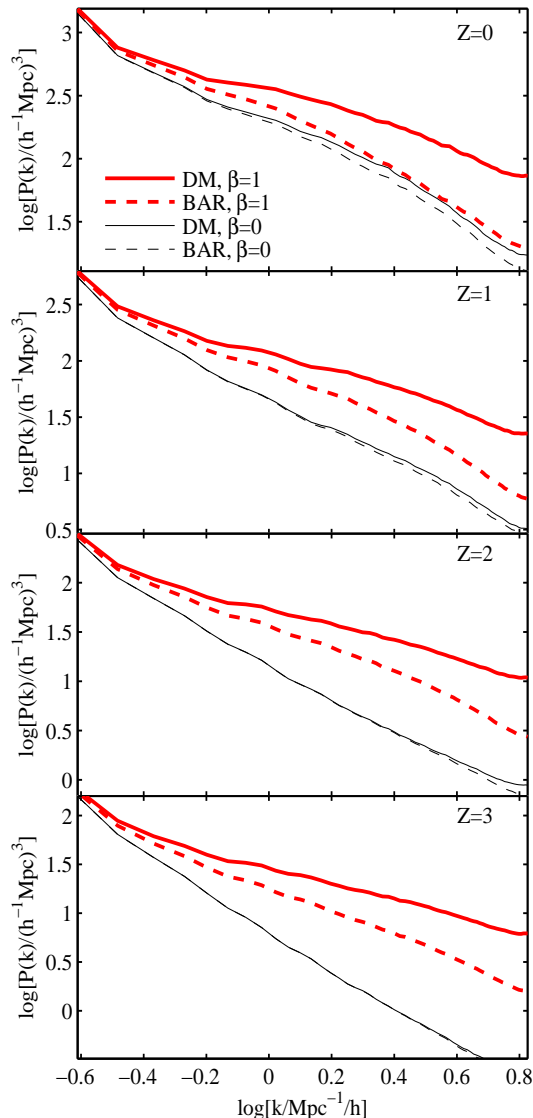
FIG. 3: PS of the baryon and DM distributions for $\beta = 0$ and $\beta = 1$ at the redshifts indicated in the figure.

almost the same on scales large compared to the screening length, $r_s = 1\,h^{-1}\mathrm{Mpc}$, while ReBEL considerably increases the clustering of the DM on smaller scales. In the standard scenario the baryon PS (thin dashed) closely follows that of the DM (thin solid) at all redshifts, while in the ReBEL scenario the baryon PS (thick dashed) falls below the DM curve (thick solid). The baryons in the ReBEL simulation are significantly more clustered than in the standard model at higher redshifts, but at $z = 0$ the baryons in the standard and ReBEL scenarios have relaxed to quite similar PS. This evolution is illustrated in another way by the autocorrelation functions in Fig. 4.

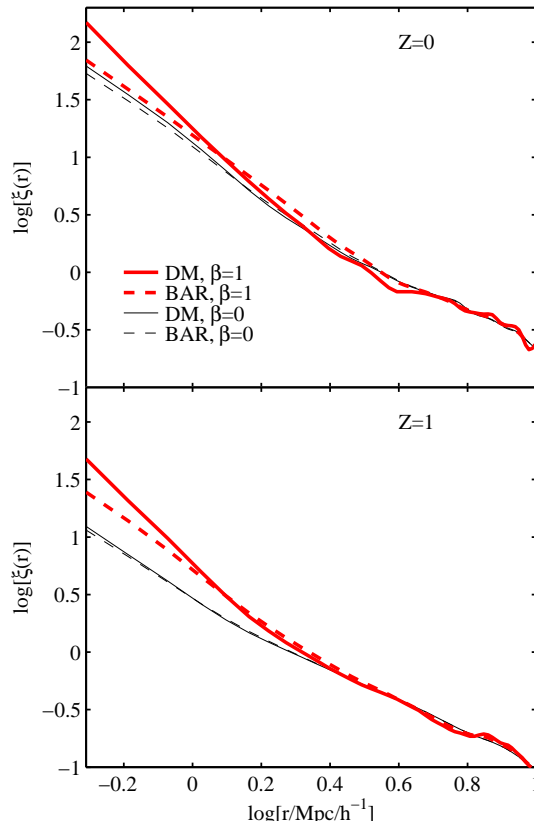Galaxy redshift surveys provide redshift distances that

FIG. 4: Autocorrelation functions for the two components of the two simulations at the current epoch and redshift $z = 1$.

differ from real distances by the radial velocity term, breaking the isotropy of the position correlation function, thus offering a probe of the peculiar velocity field and through that the cosmological model. Fig. 5 shows the redshift space correlation function $\xi^s(r_p, \pi)$ as a function of the redshift space separation r_p perpendicular to the line of sight and π parallel to the line of sight [63, 64], but here computed for the DM in the standard and ReBEL cases. Random motions on small scales cause the spike at $r_p \approx 0$. It is more pronounced for $\beta = 1$, reflecting the stronger small-scale clustering. On scales larger than $r_s = 1\,h^{-1}\mathrm{Mpc}$, the contours have a similar pattern. We cannot explore the anisotropy of the redshift space correlation functions of halos and mock HOD galaxies because the anisotropy is sensitive to peculiar motions and our simulations are of insufficient dynamical range to model these motions properly.

2. The Lyα forest

The Lyα forest in QSO spectra is caused by resonant scattering of QSO light by diffuse atomic hydrogen along the line of sight. This is an important tracer of the distribution of intergalactic baryons at high redshift [65].
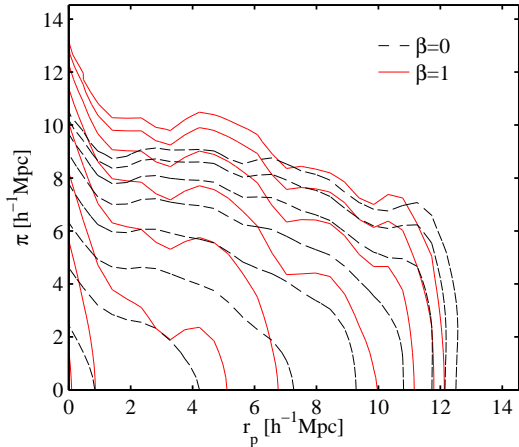
FIG. 5: Contours of the DM redshift space correlation function $\xi^s(r_p, \pi)$ as function of perpendicular (r_p) and parallel (π) separations. The contours are spaced by intervals of 0.2 in $\log(\xi^s)$, starting with $\log(\xi^s) = -1.9$ at the outermost contour.

The standard ΛCDM scenario matches well the observed one-dimensional (1D) PS derived from the forest [66]. We present here a preliminary assessment of whether or not the ReBEL scenario can also match the 1D PS. This is an interesting test because it probes the baryon distribution at epochs where the ReBEL scenario significantly differs from the standard model (Fig. 3).

The normalized transmitted flux (hereafter flux) in the Lyα absorption spectrum is

$$F = \exp(-\tau), \qquad \tau = \mathcal{A}\rho_{\text{gas}}^{\alpha}. \qquad (4)$$

The optical depth τ depends on the mass density ρ_{gas} in baryons, plasma plus neutral, where α is a parameter in the range 1.5 to 2, depending on the photoionization history, and the proportionality factor $\mathcal{A}$, which depends on the intensity of the ionizing background [67], is given by [68]

$$\mathcal{A}(z) \approx \qquad (5)$$
$$0.61 \left(\frac{300\,\text{km s}^{-1}\,\text{Mpc}^{-1}}{H(z)}\right) \left(\frac{\Omega_{\text{bar}}h^2}{0.02}\right)^2 \times \ldots$$
$$\left(\frac{\Gamma_{\text{phot}}}{10^{-12}\,\text{s}^{-1}}\right)^{-1} \left(\frac{\hat{T}}{1.5 \times 10^4\,\text{K}}\right)^{-0.7} \left(\frac{1+z}{4}\right)^6.$$

Here Ω_{bar} is the baryon density parameter and Γ_{phot} is the photoionization rate per hydrogen atom.

We consider the Lyα 1D PS of F for wavenumbers in the range

$$0.3\,\text{h Mpc}^{-1} \lesssim k \lesssim 4\,\text{h Mpc}^{-1}. \qquad (6)$$

The lower bound is set by fluctuations in the continuum [69] and the upper bound by contamination by metal lines [70, 71]. We compare the simulations to the observed Lyα 1D PS at redshift $z \approx 3$.

To estimate ρ_{gas} as a function of position in the simulations we interpolate the baryon particle positions by a cell-in-cloud (CIC) procedure to derive the gas density field on a 256^3 uniform cubic grid in the simulation box. This grid has a Nyquist frequency close to the upper limit beyond which the flux PS is contaminated by metal lines. The density field is then deconvolved by the CIC kernel $\text{sinc}^2(k_x L/N_g)\,\text{sinc}^2(k_y L/N_g)\,\text{sinc}^2(k_z L/N_g)$ where L is the box length, and N_g is the number of cells on the side. The density field along 256^2 sight lines is then smoothed with a 1D Gaussian window of width σ_f. This smoothing is temperature-dependent and is introduced in order to mimic temperature broadening [66]. It will be treated here as a free parameter. The resolution of the simulations is insufficient to model the PS properly at wavenumbers close to the upper limit in Eq 6, so we degrade the observations to conform with the resolution of our simulations. We convolve the observed PS with a Gaussian window [69],

$$P_F(k) \Rightarrow P_F(k)\,\exp\left(k^2/k_\sigma^2\right), \qquad (7)$$

where $k_\sigma = \sqrt{8\ln 2}/\text{FWHM}$. We use a FWHM equivalent to the mean separation between gas particles. In addition, to avoid dealing with continuum fitting effects, we truncate the transmitted flux [66] at $F = 0.8$.
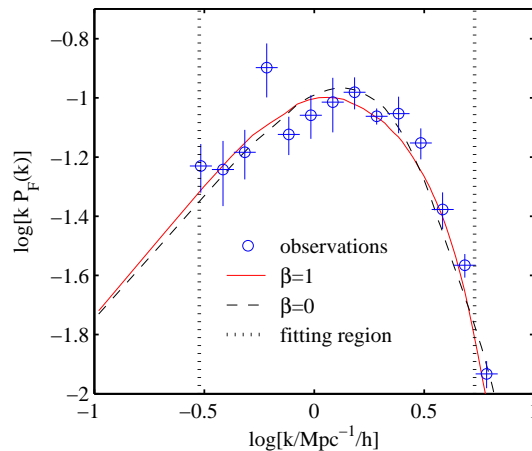

FIG. 6: The 1D Lyα flux power spectra computed from the $\beta = 0$ and $\beta = 1$ simulations are shown as the dashed and solid lines respectively. The observed PS is shown as circles overlaid with crosses representing the error bars and bin sizes. The vertical dotted lines correspond to the bounds in Eq. 6.

The dimensionless measure $k\,P_F(k)$ of the observed 1D PS of the Lyα transmitted flux compiled in [70] is plotted as the open circles in Fig. 6. The curves show the 1D PS computed from the two simulations. The parameters in these simulated PS are, for $\beta = 0$, $\alpha = 1.99$, $\mathcal{A} = 0.48$, and $\sigma_f = 0.32\,\text{h}^{-1}\text{Mpc}$, and, for $\beta = 1$, $\alpha = 1.66$, $\mathcal{A} = 0.71$, and $\sigma_f = 0.35\,\text{h}^{-1}\text{Mpc}$. For mean ICM temperature $\hat{T} = 1.5 \times 10^4\,\text{K}$ these parameters give photoionization rates $\Gamma_{\text{phot}} = 6.9 \times 10^{-12} s^{-1}$ for $\beta = 0$

and $4.6 \times 10^{-12} s^{-1}$ for $\beta = 1$. The values of σ_f correspond to $k_f \approx 18 \, h \, \mathrm{Mpc}^{-1}$ for the broadening parameter used in [66], slightly larger than the maximum value adopted in that work.

Fig. 6 shows that both ΛCDM and ReBEL can agree with the observations within the limits of the present analysis. We caution, however, that this is a preliminary test because our simulations neither include a direct treatment of photoheating and photoionization nor they are of sufficient resolution to resolve the Jeans mass.

3. Clustering of galaxies

Galaxies form in DM halos where the gas density can reach high enough values to cool, contract, and form stars. Therefore, in contrast to the Lyα forest, which traces the baryons, the distribution of galaxies is dictated by the DM density field.
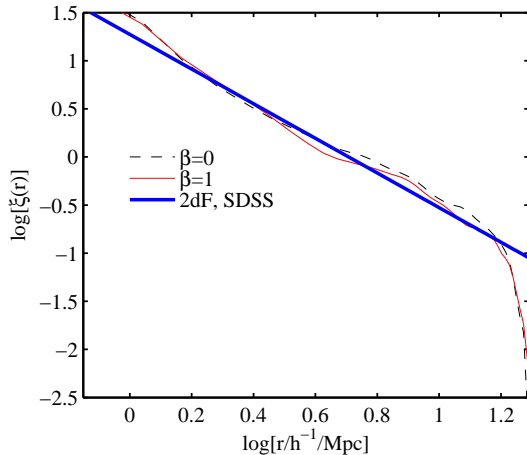

FIG. 7: Correlation functions for the positions of the HOD-placed galaxies in the $\beta = 0$ and $\beta = 1$ simulations are shown as the thin dashed and thin solid lines respectively. The observed correlation function of galaxies is derived from the 2dF and SDSS surveys.

In the simulations we populate halos with "galaxies" according to the HOD framework described in § III B. The HOD parameters for the $\beta = 0$ simulation are $\alpha = 1.13$, $M_{\min} = 3 \times 10^{11}$, and $M_1 = 8 \times 10^{12} \, h^{-1} M_\odot$. They are similar to the ones derived in [60]. The parameters for the $\beta = 1$ simulation are $M_s \simeq 1.3 \times 10^{13} \, h^{-1} M_\odot$, $\alpha = 1.13$ (as for $\beta = 0$), $\gamma = 1.8$, $M_{\min} = 2.2 \times 10^{12}$, $M_1 = 6.3 \times 10^{12} \, h^{-1} M_\odot$. In the $\beta = 1$ simulation the multiplicative factor, ζ, by which satellite distances from the halo center are increased relative to the DM distribution in the host halo is $\zeta = 4$.

The solid and dashed curves in Fig. 7 show the correlation functions of these galaxies in the two simulations. The thick solid line is the fit $\xi = (r/5.1 \, h^{-1} \mathrm{Mpc})^{-1.8}$ to the observed correlation function extracted from Fig. 11
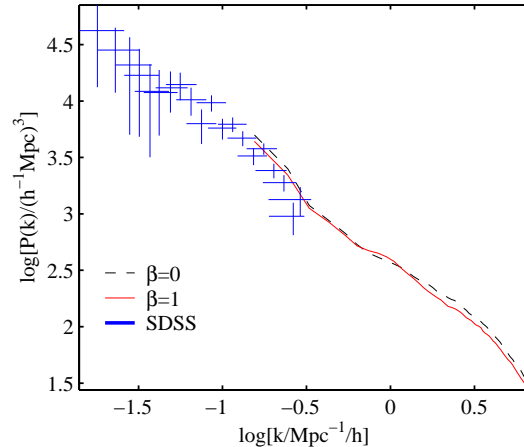

FIG. 8: Galaxy PS from HOD galaxies in the simulations and in the SDSS galaxy survey.

in [59]. In the range of separations shown here the correlation functions in the two simulations, with the adopted HOD parameters, agree reasonably well with each other with what is observed. The alternative view from the galaxy PS is shown in Fig. 8. The observed galaxy PS is taken from the SDSS galaxy redshift survey (table 2 of [72]).

An important test not examined here is the shape of the correlation function of the simulated galaxies on smaller scales, where ReBEL may be expected to have a larger effect. That will require simulations with better resolution.

In the range of galaxy separations we can explore the fit of the position correlation function of the ReBEL simulation HOD galaxies to the observed galaxy correlation requires HOD parameter $\zeta = 4$. That is, ReBEL requires that the distribution of satellite galaxies is considerably more extended than the DM in the host halo. This is in contrast to the standard cosmology in which only a mild bias, or none at all (as in this work), is needed to match the galaxy correlation function. In high resolution simulations of standard ΛCDM the distribution of the DM sub-halo population is more extended than the distribution of diffuse DM in the host halo [73–78]. That is, HOD satellite galaxies which trace the general DM distribution cannot be associated directly with the sub-halo population. We may expect that sub-halos in the ReBEL scenario are also more extended than the DM distribution in the host halo, but that remains to be checked, along with the possibility that satellites galaxies could be more directly related to sub-halos in the ReBEL scenario.
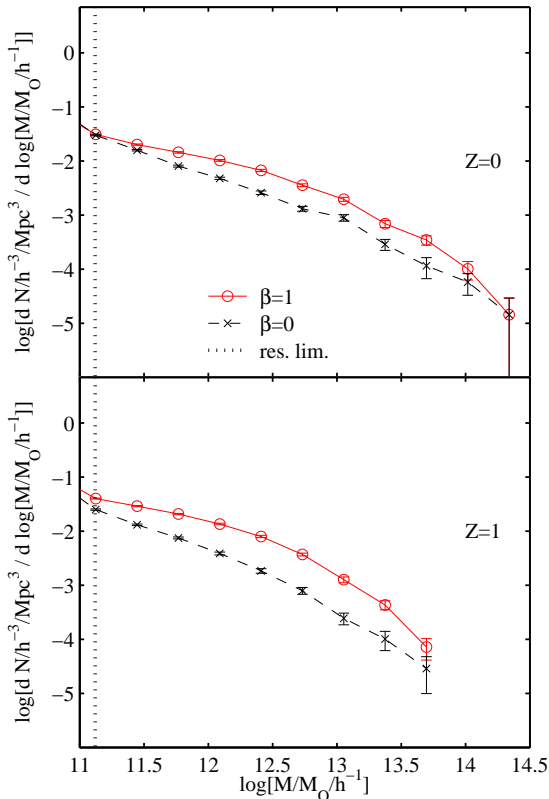
FIG. 9: Mass function of halos in the $\beta = 0$ and $\beta = 1$ simulations at redshifts $z = 0$ and $z = 1$, for DM particles only. The vertical dashed line marks a mass of a halo containing 20 DM particles as identified by the FOF algorithm.

B. Properties of halos

1. The halo mass function

To explore the abundance of DM halos as a function of their mass we select FOF groups containing more than 20 DM particles each, giving a minimum halo mass of $1.3 \times 10^{11} \, h^{-1} M_\odot$. The mass functions expressed as the number density of halos per logarithmic mass bin are plotted in Fig. 9. The 1σ error bars are estimated by the Bootstrap resampling procedure described in [79].

The mass functions in the two simulations are nearly the same at $M \approx 10^{11} \, h^{-1} M_\odot$, which is close to the minimum halo mass we can identify. The difference between mass functions also is small at $M \approx 10^{14} \, h^{-1} M_\odot$, about the mass at $z = 0$ at which the virial radius is equal to the screening length $r_{\rm s} = 1 \, h^{-1} {\rm Mpc}$. At the still larger masses characteristic of clusters of galaxies the ReBEL force is less effective and we may expect the mass function to be less sensitive to β. Our computation box size is too small to explore this.

The mass functions in the ReBEL and standard ΛCDM simulations at the present epoch differ by a factor of

about two at $M \sim 10^{12} \, h^{-1} M_\odot$, roughly the DM mass of the Milky Way [80]. Translating this to the predicted effect on the galaxy luminosity function does not seem likely to be reliable at the present state of the art.

The difference between the mass functions is greater at redshift $z = 1$, and the mass function expressed in comoving coordinates evolves more slowly at $z < 1$ in the ReBEL scenario. As we discuss next, this agrees with the earlier completion of merging in ReBEL.
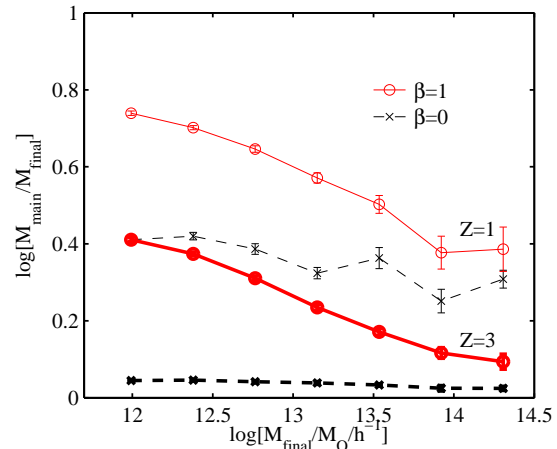

FIG. 10: Mean fractions of mass assembled by redshifts $Z = 1$ and $Z = 3$ as functions of the present halo mass in the simulations with and without ReBEL.

2. Halo Merging History

A present-day halo went through a time of intense merging activity when it acquired a significant fraction of its present mass. For a measure of when this happened we identify in each DM halo at $z = 0$ the particles belonging to the most massive progenitor (MMP) at redshifts $z = 1$ and $z = 3$. Fig. 10 shows the average ratios of the mass of the MMP to the present halo mass, $M_{\rm final}$, as a function of $M_{\rm final}$. The 1σ error-bars are estimated by Bootstrap re-sampling.

The figure indicates that $z = 1$ a halo with the present mass $10^{12} \, h^{-1} M_\odot$ typical of the Milky Way has assembled on average 75% of its mass in the ReBEL model with $\beta = 1$, and about half that in the standard model with $\beta = 0$. At $z = 3$ a halo now typical of the Milky Way has assembled 40% of its mass in the ReBEL model, while at $\beta = 0$ the MMP typically contains fewer than the limiting 20 particles needed for the FOF halo identifications. Similar results are reported by [81]. This effect is strongest for halos with masses typical of galaxies and it nearly disappears at masses typical of rich clusters, where it will be recalled that the virial radius exceeds the screening length $r_{\rm s}$. As discussed in § II, the earlier assembly of DM halos in ReBEL with $\beta = 1$ may play an important role in resolving issues of galaxy formation.

3. Halo Mass Profiles

Here we consider the DM mass density as a function of radius in halos at $z = 0$ that satisfy the convergence criteria [82] that the two-body relaxation time within the studied radius is much longer than the Hubble time, the smoothing length of the particles does not allow two-body accelerations to be larger than the mean field acceleration, and there are at least 50 particles within the innermost radius studied. That leads us to examine halos containing each at least 2500 particles identified in the FOF algorithm. For each halo we calculate the spherically averaged mass profile centered on the most bound particle in the halo. Here and in what follows we present the mean density $\rho(< r)$ of mass within radius r, rather than the density at radius r, to suppress the noise from the limited numbers of particles.
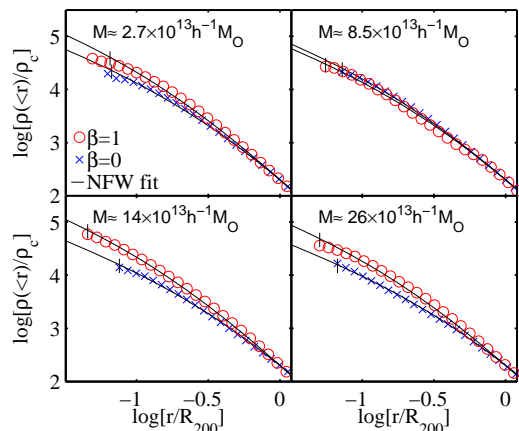

FIG. 11: Mass density runs at $z = 0$ in both simulations for four randomly chosen halos at the indicated masses. The short vertical lines mark the innermost radii that could be studied within the convergence requirements. The curves are fits to the NFW form.

Mean density profiles measured for four halos in each simulation are shown in Fig. 11. The inner vertical lines attached to each profile indicate the minimum radius, $r_{\min}$, above which the convergence criteria are satisfied.

The curves in Fig. 11 are integrals of the NFW form [83]

$$\rho(r) = \frac{\rho_0 r_{200}^3}{C_{\mathrm{NFW}} r (r_{200} + C_{\mathrm{NFW}} r)^2}. \tag{8}$$

For each halo in the figure we compute the radius r_{200} within which the mean halo density is 200 times the critical density, ρ_c. Then the concentration parameter C_{NFW} is adjusted to fit the mass density run (where ρ_0 is required to make the mean density within r_{200} equal to $200\rho_c$).

We use two measures of the performance of the NFW profile under a ReBEL force. The first is a 'Fit Error'

parameter

$$\text{Fit Error} \propto \log \left[\frac{1}{\triangle R} \int \left(\log \rho / \rho_{\mathrm{NFW}} \right)^2 \, \mathrm{d}r \right]. \tag{9}$$

The integration is from $r_{\min}$ to r_{200}, ρ is the measured density within r, ρ_{NFW} is the fitted NFW density, and $\triangle R \equiv r_{200} - r_{\min}$. The second measure is a 'Relaxed' parameter.

$$\text{Relaxed} = \log r_{200} / r_{\mathrm{cm}} \tag{10}$$

where r_{cm} is the distance of the center of mass of the FOF-group from its most bound particle. The more spherical the halo the larger its 'Relaxed' parameter.
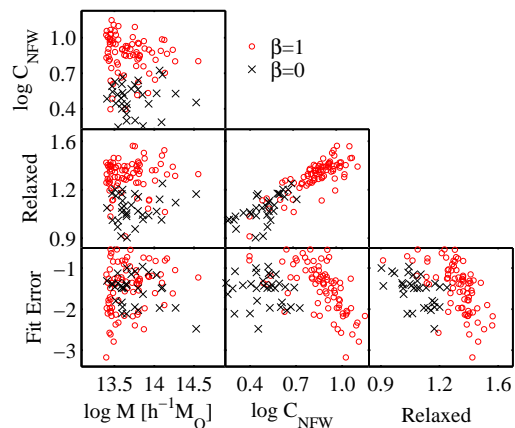

FIG. 12: Correlations of halo properties for standard and ReBEL model halos.

Fig. 12 assesses the correlations between pairs of these halo structure parameters at $z = 0$. Circles and crosses correspond to $\beta = 1$ and $\beta = 0$. The three panels in the bottom row are scatter plots of the 'Fit-Error' parameter versus the halo mass M, the concentration parameter C_{NFW} in Eq. 8, and the 'Relaxed' parameter in Eq. 10. These panels indicate the NFW profile about equally well matches the halo mass profile in both simulations. This agrees with the findings of [81], who used a different measure than Eq. 9. These scatter plots also make the possibly important point that the ReBEL scenario produces halos that are more relaxed and more concentrated.

4. Baryonic mass fraction in halos

The baryon mass fraction f_b is the ratio of the mass density in baryons to the mass density in baryons plus dark matter, normalized to unity at the cosmic mean Ω_b / Ω_m. We consider here the measured [43, 44] and computed values of f_b in galaxies and systems of galaxies.

In the largest clusters of galaxies f_b is close to unity [84, 85]; these systems are tightly enough bound that
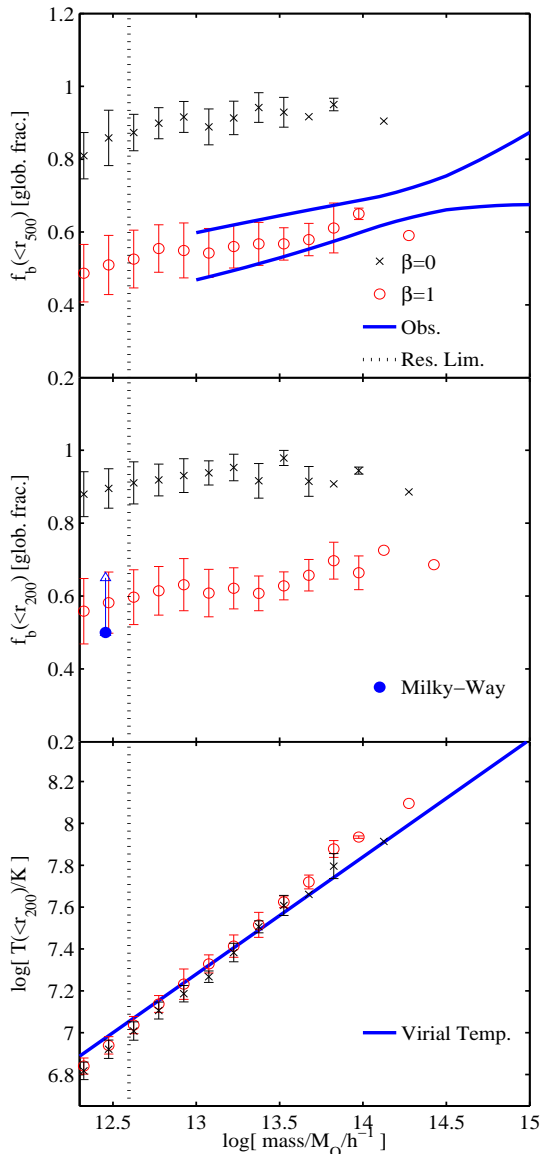
radiative losses and star formation processes, which could increase the mass fraction in the simulated haloes by 10% [90, 91]. Baryonic energy dissipation through radiation increases the total baryonic fraction in haloes because gas flows deeper into haloes to replace cooled gas.

The top and middle panels in Fig. 13 show the computed means of the baryon mass fractions f_b within distances r_{500} and r_{200} from the most bound particle in halos at $z = 0$ in our simulations with $\beta = 0$ (black crosses) and $\beta = 1$ (red circles). The horizontal axis is the DM halo mass within r_{500} for the top panel and r_{200} for the center panel. The vertical dotted lines mark the mass in a halo containing a minimum mass equal to the sum of 500 DM and 500 baryonic particles, the threshold for reliable estimation of mass fractions in simulations suggested by the convergence studies of [92, 93]. The computed f_b in our standard ΛCDM simulation agrees with previous studies [92, 94]. We find that the variation of f_b with redshift is weak in both the $\beta = 1$ and $\beta = 0$ simulations (c.f. [90–92, 95, 96]).

The bottom panel of the figure shows the mean gas temperature within r_{200} as a function of the DM mass within r_{200}. The solid line is computed from the virial relation ($T \sim GM/r_{200}$). Halos in the ReBEL (circles) and standard (crosses) simulations both closely follow the virial relation.

The top panel of Fig. 13 illustrates the well-established evidence that in galaxies and groups of galaxies roughly half the baryons are missing. At halo mass $\sim 10^{12} M_\odot$ the plasma temperature is $\sim 10^6$ K, cool enough to escape detection as an X-ray source. In galaxies at this mass and lower the missing baryons could be in the DM halo as a galactic corona [97]. At larger mass the missing baryons have to have been removed from their DM halos, perhaps by galactic superwinds driven by supernovae and active galactic nuclei [98–101]. The ReBEL scenario adds another possibility, that differential acceleration of baryons and DM has separated some baryons from their halos.

The weight of evidence for or against ReBEL from the baryon mass fraction f_b in galaxies and systems of galaxies depends on the quite uncertain astrophysics of baryon winds. If these processes were effective in suppressing f_b then ReBEL could make f_b unacceptably small. If winds proved to be ineffective it would argue for ReBEL at about the parameter values for the DM force we have adopted, for the observed and computed baryon fractions agree in our ReBEL simulation. The ReBEL prediction for clusters, which have close to the cosmic baryon fraction, requires larger simulations. The blue filled circle in the middle panel in Fig. 13 shows that the observed baryon fraction in the Milky Way is well below the ΛCDM case and agrees with ReBEL. This is particularly interesting because the relatively low mass of the central black hole in our galaxy might argue against removal of the baryons by a superwind. But the Milky Way is at about the mass threshold where the missing baryons may be in a corona cool enough to be detected

FIG. 13: Baryonic mass fraction f_b versus DM halo mass. Top and middle panels, respectively, correspond to masses within r_{500} and r_{200}. Solid curves in the top panel are $\pm 1\sigma$ limits on the mass fraction from recent observations. The bottom panel shows the mean gas temperature within r_{200} versus the DM halo mass within r_{200}; the solid line is the virial temperature relation.

they have resisted large loss of baryons. The heavy blue solid curves in the top panel in Fig. 13 are the $\pm 1\sigma$ limits on observed baryon fractions in lower mass halos. This includes the mass in X-ray emitting plasma, and the mass in stars, as given in parametric form in [86]. Two adjustments are made to these components. First, the stellar mass is increased by 11% to take account of the contribution from intracluster light [87–89]. Second, f_b is reduced by 10%, as a method to overcome the systematic errors arising in our simulations, which do not model
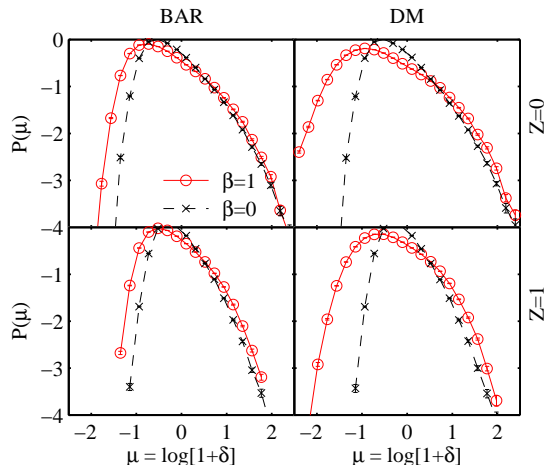
as an X-ray source.

FIG. 14: Probability distributions of the densities in baryons and DM smoothed by a top-hat window of radius $1.5\,\mathrm{h}^{-1}\mathrm{Mpc}$

C. Void properties

Fig. 14 shows the effect of ReBEL on the probability distribution functions of the mass densities in baryons and DM averaged within randomly placed top-hat windows of radius $1.5\,\mathrm{h}^{-1}\mathrm{Mpc}$. The densities are normalized to the cosmic means at the computed redshifts, $z = 1$ and $z = 0$, as the density contrast $\delta = \rho/\bar{\rho} - 1$. ReBEL more efficiently evacuates low density regions, as previously demonstrated [1]. Here we explore in more detail the effects of ReBEL on voids.

We define a void in the simulation as a spherical region of radius R with average density contrast δ_{v}. We identify voids in the distribution of particles in a simulation as follows. We derive a density field by CIC interpolation of the points to a cubic grid with 128 cells on the side. The density field is then smoothed with a Top-Hat window with radius large enough that there are no grid points with density contrast less than δ_{v}. The width of the Top-Hat window is then gradually decreased until a single grid point with $\delta = \delta_{\mathrm{v}}$ is encountered. This grid point is taken to be the center of the largest void and its size is the window radius R. The filtering radius is further decreased to locate successively smaller voids, excluding those overlapping with the larger, already identified, voids [102].

Table I lists counts of voids in the ΛCDM and ReBEL simulations for two ranges of values of the void radii and the threshold density contrast δ_v. ReBEL considerably increases the numbers of voids, as also illustrated in Fig. 14, and the effect on the number of larger voids is even more pronounced at the lower threshold $\delta_{\mathrm{v}} = -0.9$. The number of smaller voids is smaller at $\delta_{\mathrm{v}} = -0.8$ because many of the small voids at $\delta_{\mathrm{v}} = -0.9$ become parts

TABLE I: Counts of Voids

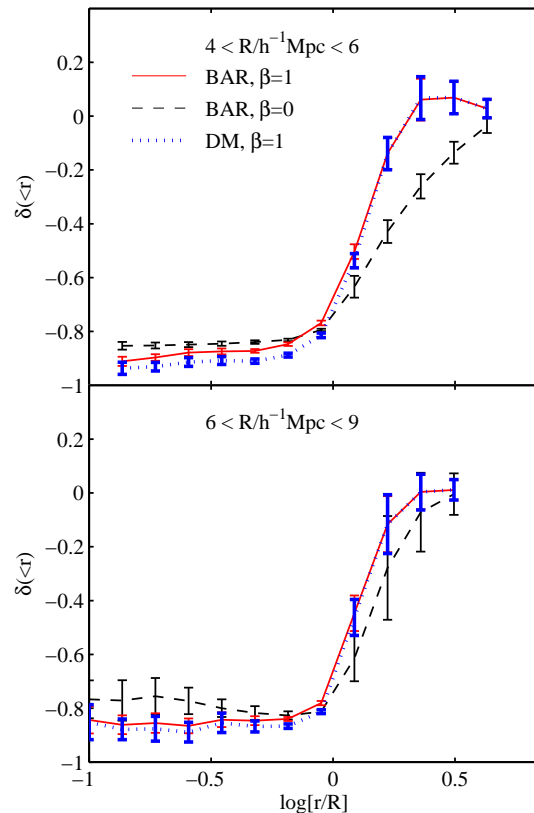| β	δ_v	$4 < R < 6^a$	$6 < R < 9^a$
0	-0.8	36	5
1	-0.8	54	16
0	$-.09$	4	0
1	$-.09$	69	6

^{a}unit $= \mathrm{h}^{-1}\mathrm{Mpc}$

FIG. 15: Void mean density within radius r at redshift $z = 0$ for large (bottom) and small voids (top). The void radius is R.

of larger voids at $\delta_{\mathrm{v}} = -0.8$.

We represent the mass distribution within a void as the density contrast computed from the mass contained within distance r from its center. This measure is less noisy than the local mass density profile. Fig. 15 shows means of the void profiles for small (top panel) and large voids (bottom). ReBEL reduces the DM density in the central regions and produces a steeper density gradient at the void edge. Both effects are more pronounced in smaller voids, consistent with [103]. This could ease the tension between the observations that indicate that small void profiles have a sharper transition into the outer regions than what appears in ΛCDM simulations [102].

The DM particle mass in our simulations is too large to allow an analysis of the distribution of low mass halos in

voids. We can note, however, that the distinct suppression of the mean DM density in voids is in the wanted direction to suppress the numbers of void galaxies, while the lesser suppression of baryons may be more relevant for the density of diffuse plasma in voids.
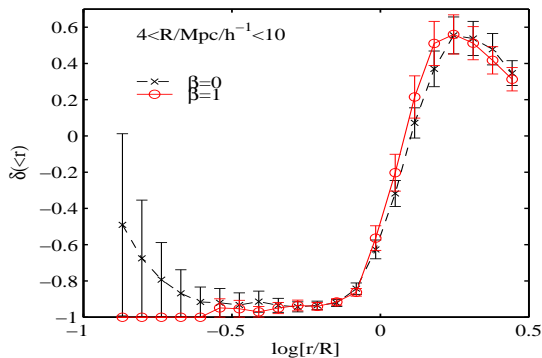

FIG. 16: Mean density contrast of HOD galaxies in voids.

Figs. 16 and 17 show checks that ReBEL can match the void size distribution and the distributions of bright galaxies in voids as well as the standard model. The galaxies are modeled for absolute magnitude limit -19.5 in the r band. The HOD parameters were tuned so that similar void properties for these galaxies are obtained in ReBEL and the standard cosmology. The vertical axis in Figs. 16 is the mean HOD galaxy number averaged within radius r and scaled to the void radius R. Fig.17 shows the number of voids in our simulations as a function of the void radius, using $\delta_v = -0.8$. We conclude from the consistency of results for $\beta = 0$ and $\beta = 1$ in the statistics in Figs. 16 and 17 that at the level of our simulations the bright galaxy distribution does not a usefully discriminate between ΛCDM and ReBEL.

V. DISCUSSION

We have considered the effect of ReBEL, a long-range force of attraction acting on the dark matter alone. The force is modeled by Eq. 1 with $\beta = 1$, meaning the strength is the same as gravity, and screening length $r_s = 1\,h^{-1}\mathrm{Mpc}$, meaning it has no influence on the cosmological tests but can have interesting effects on galaxies.

ReBEL with the parameters adopted here satisfies the known constraints from properties of satellites of the Milky Way, as discussed elsewhere [2, 4, 7], but this certainly requires closer analysis. Within the framework of the Halo Occupation Distribution (HOD) model for galaxies we have shown that ReBEL fits the measured galaxy correlation function at separations greater than about one megaparsec as well as does the standard
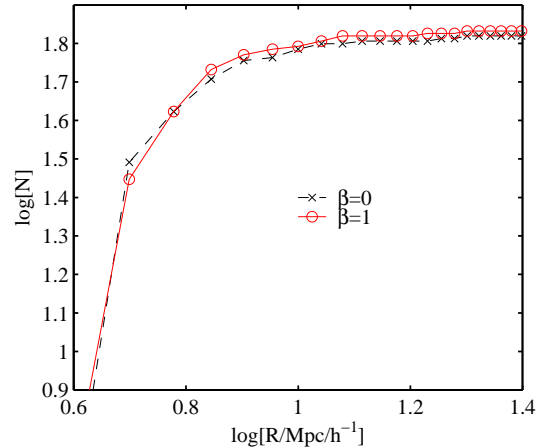

FIG. 17: Number of voids smaller than R and larger than $4\,h^{-1}\mathrm{Mpc}$.

ΛCDM cosmology. Checking galaxy clustering on smaller scales will require larger simulations.

We have also concluded that ReBEL can account for the properties of the Lyman-Alpha forest about as well as ΛCDM, at the level of semi-analytic methods [66, 104]. Again, this requires deeper analysis, including resolution of the Jeans mass of the intergalactic medium and an explicit treatment of photoionization and photoheating by the ionizing radiation background.

Fig. 13 shows that ReBEL offers a natural explanation of the missing baryons in galaxies and groups of galaxies. This may be important because the hypothesis that superwinds removed the baryons from isolated galaxies and loose groups does not have a secure theoretical or empirical basis.

Fig. 10 shows that ReBEL substantially advances the redshift of assembly of the bulk of the mass of a galaxy. This may be important in resolving the puzzle of disk-dominated galaxies [105]. In ΛCDM inefficient star formation allows development of dwarf pure disk galaxies [106], but that approach would make the disk of the Milky Way unacceptably young [107]. ReBEL would help by assembling the parts of a galaxy earlier, and assembling a lower baryon mass fraction. Much better resolution simulations will be needed to explore whether ReBEL can promote formation of significant numbers of bulge-free spiral galaxies with acceptable galaxy rotation curves, along with appreciable numbers of large red galaxies at high redshifts.

Earlier structure formation may also be relevant to the measurements of polarization of the cosmic microwave background radiation that indicate a significant reionization by redshift $z \sim 11$, implying early structure formation. Star formation in the ΛCDM with $\sigma_8 \approx 0.9$ could be early enough to account for such early reionization, but extreme efficiency of UV photon production by early structures is needed for $\sigma_8 \approx 0.8$, the value favored by WMAP data [40]. ReBEL may relieve this condition.

Earlier assembly is accompanied by more massive DM halos at the present epoch. The effect is not large, however, as illustrated in Fig. 9, and it would seem to be a difficult challenge to translate this into a test of ReBEL from the galaxy luminosity function.

Figure 15 shows the depression of the DM mass density within voids, and the lesser suppression of the baryon mass density. This is in the wanted direction of resolving the void over-population problem, but larger simulations will be needed to estimate the effect of the lower DM density on the formation of low mass DM halos. Finally, we illustrate in Fig. 12 the formation of larger halo NFW concentrations in ReBEL, which is in the direction suggested by recent measurements [24–27, 108].

[1] A. Nusser, S. S. Gubser, and P. J. Peebles, Phys. Rev. D **71**, 083505 (2005), arXiv:astro-ph/0412586.

[2] M. Kesden and M. Kamionkowski, Phys. Rev. D **74**, 083007 (2006), arXiv:astro-ph/0608095.

[3] W. A. Hellwing and R. Juszkiewicz, ArXiv e-prints (2008), 0809.1976.

[4] J. A. Keselman, A. Nusser, and P. J. E. Peebles, ArXiv e-prints (2009), 0902.3452.

[5] V. Springel, MNRAS **364**, 1105 (2005), arXiv:astro-ph/0505010.

[6] G. R. Farrar and P. J. E. Peebles, ApJ **604**, 1 (2004), arXiv:astro-ph/0307316.

[7] J. A. Frieman and B. Gradwohl, Science **260**, 1441 (1993).

[8] R. A. Ibata, G. Gilmore, and M. J. Irwin, Nature **370**, 194 (1994).

[9] R. Bean, É. É. Flanagan, I. Laszlo, and M. Trodden, Phys. Rev. D **78**, 123514 (2008), 0808.1105.

[10] L. Perivolaropoulos, ArXiv e-prints (2008), 0811.4684.

[11] A. Klypin, A. V. Kravtsov, O. Valenzuela, and F. Prada, ApJ **522**, 82 (1999), arXiv:astro-ph/9901240.

[12] B. Moore, in *20th Texas Symposium on relativistic astrophysics*, edited by J. C. Wheeler & H. Martel (2001), vol. 586 of *American Institute of Physics Conference Series*, pp. 73–82.

[13] P. Madau, J. Diemand, and M. Kuhlen, ApJ **679**, 1260 (2008), 0802.2265.

[14] J. D. Simon and M. Geha, ApJ **670**, 313 (2007), 0706.0516.

[15] L. E. Strigari, J. S. Bullock, M. Kaplinghat, J. Diemand, M. Kuhlen, and P. Madau, ApJ **669**, 676 (2007), 0704.1817.

[16] P. J. E. Peebles, ApJ **557**, 495 (2001), arXiv:astro-ph/0101127.

[17] S. Gottlöber, E. L. Łokas, A. Klypin, and Y. Hoffman, MNRAS **344**, 715 (2003), arXiv:astro-ph/0305393.

[18] D. M. Goldberg and M. S. Vogeley, ApJ **605**, 1 (2004), arXiv:astro-ph/0307191.

[19] P. J. E. Peebles, Nuovo Cimento B Serie **122**, 1035 (2007), 0710.5036.

[20] A. V. Tikhonov and A. Klypin, MNRAS **395**, 1915 (2009), 0807.0924.

[21] I. D. Karachentsev, V. E. Karachentseva, W. K. Huchtmeier, and D. I. Makarov, AJ **127**, 2031 (2004).

[22] M. J. Meyer, M. A. Zwaan, R. L. Webster, L. Staveley-Smith, E. Ryan-Weber, M. J. Drinkwater, D. G. Barnes, M. Howlett, V. A. Kilborn, J. Stevens, et al., MNRAS **350**, 1195 (2004), arXiv:astro-ph/0406384.

[23] L. Peebles and F. Nusser (????).

[24] T. Broadhurst, M. Takada, K. Umetsu, X. Kong, N. Arimoto, M. Chiba, and T. Futamase, ApJL **619**, L143 (2005), arXiv:astro-ph/0412192.

[25] K. Umetsu and T. Broadhurst, ApJ **684**, 177 (2008), 0712.3441.

[26] T. Broadhurst, K. Umetsu, E. Medezinski, M. Oguri, and Y. Rephaeli, ApJL **685**, L9 (2008), 0805.2617.

[27] D. Lemze, R. Barkana, T. J. Broadhurst, and Y. Rephaeli, MNRAS **386**, 1092 (2008), 0711.3908.

[28] K. R. Stewart, J. S. Bullock, R. H. Wechsler, A. H. Maller, and A. R. Zentner, ApJ **683**, 597 (2008), 0711.5027.

[29] L. Mayer, F. Governato, and T. Kaufmann, Advanced Science Letters **1**, 7 (2008), 0801.3845.

[30] S. M. Weinmann, F. C. van den Bosch, X. Yang, and H. J. Mo, MNRAS **366**, 2 (2006), arXiv:astro-ph/0509147.

[31] R. F. G. Wyse, in *Galaxy Disks and Disk Galaxies*, edited by J. G. Funes & E. M. Corsini (2001), vol. 230 of *Astronomical Society of the Pacific Conference Series*, pp. 71–80.

[32] J. Kormendy and D. B. Fisher, in *Revista Mexicana de Astronomia y Astrofisica Conference Series*, edited by S. Torres-Peimbert & G. MacAlpine (2005), vol. 23 of *Revista Mexicana de Astronomia y Astrofisica Conference Series*, pp. 101–108.

[33] S. A. Wright, J. E. Larkin, D. R. Law, C. C. Steidel, A. E. Shapley, and D. K. Erb, ApJ **699**, 421 (2009), 0810.5599.

[34] D. W. Hogg, M. R. Blanton, J. Brinchmann, D. J. Eisenstein, D. J. Schlegel, J. E. Gunn, T. A. McKay, H.-W. Rix, N. A. Bahcall, J. Brinkmann, et al., ApJL **601**, L29 (2004), arXiv:astro-ph/0307336.

[35] M. Bernardi, R. C. Nichol, R. K. Sheth, C. J. Miller, and J. Brinkmann, AJ **131**, 1288 (2006), arXiv:astro-ph/0509360.

[36] M. J. Disney, J. D. Romano, D. A. Garcia-Appadoo, A. A. West, J. J. Dalcanton, and L. Cortese, Nature **455**, 1082 (2008), 0811.1554.

[37] P. B. Nair, S. van den Bergh, and R. G. Abraham (????).

[38] R. Cen, New Astronomy Review **50**, 191 (2006).

[39] A. Kogut, D. N. Spergel, C. Barnes, C. L. Bennett, M. Halpern, G. Hinshaw, N. Jarosik, M. Limon, S. S. Meyer, L. Page, et al., ApJS **148**, 161 (2003), arXiv:astro-ph/0302213.

[40] A. J. Benson, N. Sugiyama, A. Nusser, and C. G. Lacey, MNRAS **369**, 1055 (2006), arXiv:astro-ph/0512364.

[41] N. Afshordi, Y.-T. Lin, D. Nagai, and A. J. R. Sanderson, MNRAS **378**, 293 (2007), arXiv:astro-ph/0612700.

[42] H. Hoekstra, B. C. Hsieh, H. K. C. Yee, H. Lin, and M. D. Gladders, ApJ **635**, 73 (2005), arXiv:astro-ph/0510097.

[43] S. S. McGaugh, in *IAU Symposium*, edited by J. Davies and M. Disney (2008), vol. 244 of *IAU Symposium*, pp. 136–145.

[44] S. S. McGaugh, J. M. Schombert, W. J. G. de Blok, and M. J. Zagursky, ArXiv e-prints (2009), 0911.2700.

[45] I. G. McCarthy, R. G. Bower, and M. L. Balogh, MNRAS **377**, 1457 (2007), arXiv:astro-ph/0609314.

[46] M. Baldi, V. Pettorino, G. Robbers, and V. Springel, ArXiv e-prints (2008), 0812.3901.

[47] M. Baldi, ArXiv e-prints (2009), 0906.5353.

[48] A. Silvestri and M. Trodden, Reports on Progress in Physics **72**, 096901 (2009), 0904.0024.

[49] J. Kripfganz and H. Perlt, Classical and Quantum Gravity **5**, 453 (1988).

[50] R. Brandenberger and C. Vafa, Nuclear Physics B **316**, 391 (1989).

[51] S. S. Gubser and P. J. E. Peebles, Phys. Rev. D **70**, 123510 (2004), arXiv:hep-th/0402225.

[52] J. Bovy and G. R. Farrar, Phys. Rev. D **102**, 101301 (2009), 0807.3060.

[53] C. W. Misner, K. S. Thorne, and J. A. Wheeler, *Gravitation* (1973).

[54] S. M. Carroll, S. Mantry, M. J. Ramsey-Musolf, and C. W. Stubbs, Physical Review Letters **103**, 011301 (2009), 0807.4363.

[55] J. Dunkley, E. Komatsu, M. R. Nolta, D. N. Spergel, D. Larson, G. Hinshaw, L. Page, C. L. Bennett, B. Gold, N. Jarosik, et al., ApJS **180**, 306 (2009), 0803.0586.

[56] J. M. Bardeen, J. R. Bond, N. Kaiser, and A. S. Szalay, ApJ **304**, 15 (1986).

[57] M. Davis, G. Efstathiou, C. S. Frenk, and S. D. M. White, ApJ **292**, 371 (1985).

[58] G. Kauffmann, A. Nusser, and M. Steinmetz, MNRAS **286**, 795 (1997), arXiv:astro-ph/9512009.

[59] A. V. Kravtsov, A. A. Berlind, R. H. Wechsler, A. A. Klypin, S. Gottlöber, B. Allgood, and J. R. Primack, ApJ **609**, 35 (2004), arXiv:astro-ph/0308519.

[60] I. Zehavi, Z. Zheng, D. H. Weinberg, J. A. Frieman, A. A. Berlind, M. R. Blanton, R. Scoccimarro, R. K. Sheth, M. A. Strauss, I. Kayo, et al., ApJ **630**, 1 (2005), arXiv:astro-ph/0408569.

[61] R. Mandelbaum, U. Seljak, R. J. Cool, M. Blanton, C. M. Hirata, and J. Brinkmann, MNRAS **372**, 758 (2006), arXiv:astro-ph/0605476.

[62] C. Adami, A. Mazure, P. Katgert, and A. Biviano, A&A **336**, 63 (1998).

[63] M. Davis and P. J. E. Peebles, ApJ **267**, 465 (1983).

[64] P. J. E. Peebles, *Principles of physical cosmology* (1993).

[65] M. Rauch, ARA&A **36**, 267 (1998), arXiv:astro-ph/9806286.

[66] V. Desjacques and A. Nusser, MNRAS **361**, 1257 (2005), arXiv:astro-ph/0410618.

[67] T. Theuns, A. Leonard, G. Efstathiou, F. R. Pearce, and P. A. Thomas, MNRAS **301**, 478 (1998), arXiv:astro-ph/9805119.

[68] A. Nusser and M. Haehnelt, MNRAS **313**, 364 (2000), arXiv:astro-ph/9906406.

[69] L. Hui, S. Burles, U. Seljak, R. E. Rutledge, E. Magnier, and D. Tytler, ApJ **552**, 15 (2001), arXiv:astro-ph/0005049.

[70] P. McDonald, J. Miralda-Escudé, M. Rauch, W. L. W. Sargent, T. A. Barlow, R. Cen, and J. P. Ostriker, ApJ **543**, 1 (2000), arXiv:astro-ph/9911196.

[71] T.-S. Kim, M. Viel, M. G. Haehnelt, R. F. Carswell, and S. Cristiani, MNRAS **347**, 355 (2004), arXiv:astro-ph/0308103.

[72] M. Tegmark, M. R. Blanton, M. A. Strauss, F. Hoyle, D. Schlegel, R. Scoccimarro, M. S. Vogeley, D. H. Weinberg, I. Zehavi, A. Berlind, et al., ApJ **606**, 702 (2004), arXiv:astro-ph/0310725.

[73] S. Ghigna, B. Moore, F. Governato, G. Lake, T. Quinn, and J. Stadel, MNRAS **300**, 146 (1998), arXiv:astro-ph/9801192.

[74] P. Colín, A. A. Klypin, A. V. Kravtsov, and A. M. Khokhlov, ApJ **523**, 32 (1999), arXiv:astro-ph/9809202.

[75] S. Ghigna, B. Moore, F. Governato, G. Lake, T. Quinn, and J. Stadel, ApJ **544**, 616 (2000), arXiv:astro-ph/9910166.

[76] V. Springel, S. D. M. White, G. Tormen, and G. Kauffmann, MNRAS **328**, 726 (2001), arXiv:astro-ph/0012055.

[77] G. De Lucia, G. Kauffmann, V. Springel, S. D. M. White, B. Lanzoni, F. Stoehr, G. Tormen, and N. Yoshida, MNRAS **348**, 333 (2004), arXiv:astro-ph/0306205.

[78] L. Gao, G. De Lucia, S. D. M. White, and A. Jenkins, MNRAS **352**, L1 (2004), arXiv:astro-ph/0405010.

[79] J. A. Keselman and A. Nusser, MNRAS **382**, 1853 (2007), 0707.4361.

[80] W. Dehnen, D. E. McLaughlin, and J. Sachania, MNRAS **369**, 1688 (2006), arXiv:astro-ph/0603825.

[81] W. A. Hellwing, ArXiv e-prints (2009), 0911.0573.

[82] C. Power, J. F. Navarro, A. Jenkins, C. S. Frenk, S. D. M. White, V. Springel, J. Stadel, and T. Quinn, MNRAS **338**, 14 (2003), arXiv:astro-ph/0201544.

[83] J. F. Navarro, C. S. Frenk, and S. D. M. White, ApJ **490**, 493 (1997), arXiv:astro-ph/9611107.

[84] Y. Zhang, H. Böhringer, A. Finoguenov, Y. Ikebe, K. Matsushita, P. Schuecker, L. Guzzo, and C. A. Collins, A&A **456**, 55 (2006), arXiv:astro-ph/0603275.

[85] A. H. Gonzalez, D. Zaritsky, and A. I. Zabludoff, ApJ **666**, 147 (2007), 0705.1726.

[86] S. Giodini, D. Pierini, A. Finoguenov, G. W. Pratt, H. Boehringer, A. Leauthaud, L. Guzzo, H. Aussel, M. Bolzonella, P. Capak, et al., ArXiv e-prints (2009), 0904.0448.

[87] S. Zibetti, S. D. M. White, D. P. Schneider, and J. Brinkmann, MNRAS **358**, 949 (2005), arXiv:astro-ph/0501194.

[88] J. E. Krick and R. A. Bernstein, AJ **134**, 466 (2007), 0704.1664.

[89] G. Murante, M. Giovalli, O. Gerhard, M. Arnaboldi, S. Borgani, and K. Dolag, MNRAS **377**, 2 (2007), arXiv:astro-ph/0701925.

[90] A. V. Kravtsov, D. Nagai, and A. A. Vikhlinin, ApJ **625**, 588 (2005), arXiv:astro-ph/0501227.

[91] S. Ettori, K. Dolag, S. Borgani, and G. Murante, MN-RAS **365**, 1021 (2006), arXiv:astro-ph/0509024.

[92] R. A. Crain, V. R. Eke, C. S. Frenk, A. Jenkins, I. G. McCarthy, J. F. Navarro, and F. R. Pearce, MNRAS **377**, 41 (2007), arXiv:astro-ph/0610602.

[93] S. Naoz, R. Barkana, and A. Mesinger, MNRAS **399**, 369 (2009), 0906.0349.

[94] S. Gottlöber and G. Yepes, ApJ **664**, 117 (2007), arXiv:astro-ph/0703164.

[95] J. F. Navarro, C. S. Frenk, and S. D. M. White, MNRAS **275**, 720 (1995), arXiv:astro-ph/9408069.

[96] V. R. Eke, J. F. Navarro, and C. S. Frenk, ApJ **503**, 569 (1998), arXiv:astro-ph/9708070.

[97] M. Fukugita and P. J. E. Peebles, ApJ **639**, 590 (2006), arXiv:astro-ph/0508040.

[98] G. Efstathiou, MNRAS **317**, 697 (2000), arXiv:astro-ph/0002245.

[99] E. Puchwein, D. Sijacki, and V. Springel, ApJL **687**, L53 (2008), 0808.0494.

[100] R. G. Bower, I. G. McCarthy, and A. J. Benson, MN-RAS **390**, 1399 (2008), 0808.2994.

[101] R. Cen and J. P. Ostriker, ApJ **650**, 560 (2006), arXiv:astro-ph/0601008.

[102] L. Ceccarelli, N. D. Padilla, C. Valotto, and D. G. Lambas, MNRAS **373**, 1440 (2006), 0805.0797.

[103] M. C. Martino and R. K. Sheth, ArXiv e-prints (2009), 0911.1829.

[104] H. G. Bi, G. Boerner, and Y. Chu, A&A **266**, 1 (1992).

[105] R. A. C. Croft, T. Di Matteo, V. Springel, and L. Hernquist, MNRAS **400**, 43 (2009), 0803.4003.

[106] F. Governato, C. Brook, L. Mayer, A. Brooks, G. Rhee, J. Wadsley, P. Jonsson, B. Willman, G. Stinson, T. Quinn, et al., ArXiv e-prints (2009), 0911.2237.

[107] R. F. G. Wyse, in *IAU Symposium*, edited by E. E. Mamajek, D. R. Soderblom, & R. F. G. Wyse (2009), vol. 258 of *IAU Symposium*, pp. 11–22.

[108] T. Broadhurst, N. Benítez, D. Coe, K. Sharon, K. Zekser, R. White, H. Ford, R. Bouwens, J. Blakeslee, M. Clampin, et al., ApJ **621**, 53 (2005), arXiv:astro-ph/0409132.

[109] R. E. Smith, J. A. Peacock, A. Jenkins, S. D. M. White, C. S. Frenk, F. R. Pearce, P. A. Thomas, G. Efstathiou, and H. M. P. Couchman, MNRAS **341**, 1311 (2003), arXiv:astro-ph/0207664.

[110] J. A. Peacock, *Cosmological Physics* (1999).

[111] S. M. Carroll, W. H. Press, and E. L. Turner, ARA&A **30**, 499 (1992).

[112] O. Lahav, P. B. Lilje, J. R. Primack, and M. J. Rees, MNRAS **251**, 128 (1991).

Appendix A: Modification of Gadget2

For the simulation with $\beta = 0$ we used the original Gadget2 public version. For the simulations with $\beta = 1$, we modified the original code as follows: in the PM part of the code we added a second loop on top of the original. This loop evaluates the density of the DM component and transforms it into the scalar potential by convolution with the proper green function, given in k space by

$$G(k) = -\frac{4\pi G\beta}{k^2 + r_s^{-2}}. \tag{A1}$$

The tree part of the code was modified so that every tree node would include a center of charge (scalar charge, equals DM mass times β) in addition to the center of mass. A cell-opening criterion was developed, such that the relative error in the sum of the ReBEL and gravitational forces is consistent with the original relative error of the gravitational force. The ReBEL force is added in a similar way to the gravitational one, that is, by considering the first moment.

To constrain the scalar force relative error we consider the worst-case scenario, this is when we calculate the force on a DM test particle, located co-linearly with two DM particles at the opposite corners of a cubical cell of width L. The relative error is of course independent of the global interaction strength β but not on the scale length r_s. To first non-vanishing order in L/r, where r is the distance of the test particle from the center of mass/charge of the cubic cell, and up to a factor of $4/3$ the relative error is given by

$$e_s = \frac{\left(r^3 + 3r^2 r_s + 6r r_s{}^2 + 6r_s{}^3\right) L^2}{6r^2 r_s{}^2(r + r_s)} \tag{A2}$$

which goes back to the usual gravitational relative error $e_g = L^2/r^2$ for $r_s \gg r$. Since the particle is given a scalar force and a gravitational one, the total relative error is constrained by

$$e_t = \frac{e_g F_g + e_s F_s}{F_g + F_s} \tag{A3}$$

which then gives the new opening criterion as

$$e_t^n \left(F_g^n + F_s^n\right) < \alpha \left(F_g^{n-1} + F_s^{n-1}\right) \tag{A4}$$

where e_t^n, F_g^n, and F_s^n are evaluated at the nth time-step and $\alpha \ll 1$ is the bounding relative error per time step.

Appendix B: Simulation tests

The modified code was checked at the large, cosmological scales, by comparing simulations to the ReBEL linear theory with a baryonic component included (as described in App. C). This is illustrated in Fig. 18, where the linear approximation is calculated for the baryonic component PS at redshift $Z = 100$ and $Z = 3$, and for the DM component only at the latter. These calculations use no more than the measured PS of the DM at $Z = 100$, a time when the decreasing solutions have almost vanished. The linear approximation seems to fit very well the simulations at the linear scales. At smaller scales the modified code was checked by two more tests, as described in [4]. The $\beta = 0$ simulation was checked at all scales by comparing the PS shown in Fig. 3 to the PS of the corresponding GIF simulation in [109].
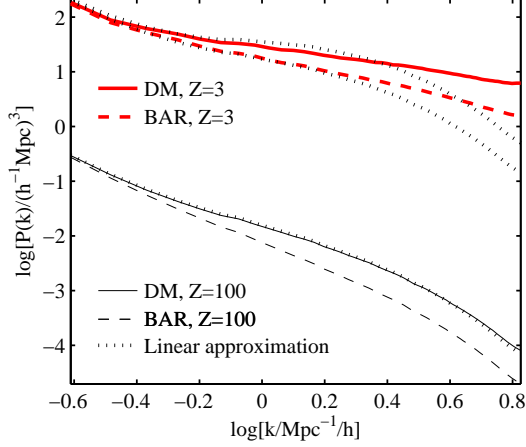
FIG. 18: Simulation PS compared with linear theory, as described in appendix C, for $\beta = 1$.

Appendix C: Linear Theory

First we write the fundamental equations of fluid motion in physical coordinates. These consist of the Euler equations,

$$\frac{d\mathbf{u}_{\mathrm{bar}}}{dt} + \frac{\nabla P}{\rho_{\mathbf{bar}}} + \nabla\phi_{\mathrm{bar}} + \nabla\phi_{\mathrm{dm}} = 0 \qquad (C1)$$

$$\frac{d\mathbf{u}_{\mathrm{dm}}}{dt} + \nabla\phi_{\mathrm{bar}} + \nabla\phi_{\mathrm{dm}} + \nabla\phi_{\mathrm{s}} = 0, \qquad (C2)$$

where $\mathbf{u}_{\mathrm{bar}}$ and $\mathbf{u}_{\mathrm{dm}}$ are the baryonic and DM velocity fields, and d/dt is the usual convective derivative, and is equal to $\partial/\partial t + \mathbf{u} \cdot \nabla$. The symbols ϕ_{bar}, ϕ_{dm}, and ϕ_{s}, represent the baryonic, DM, and scalar potential. These are given by the poison equations

$$\nabla^2\phi_{\mathrm{bar}} - 4\pi G\rho_{\mathbf{bar}} = 0 \qquad (C3)$$

$$\nabla^2\phi_{\mathrm{dm}} - 4\pi G\rho_{\mathbf{dm}} = 0 \qquad (C4)$$

$$\nabla^2\left(\phi_{\mathrm{s}} - r_{\mathrm{s}}^{-1}\right) - 4\pi G\beta\rho_{\mathbf{dm}} = 0 \qquad (C5)$$

where the last equation is a screened poison equation describing the scalar potential, and r_{s} is a function of time, and is proportional to the scale factor $a(t)$. Since this study deals with scales much larger than the Jeans scales, and the simulations are dissipation-less, we neglect the baryonic pressure and radiative cooling terms. Thus, we skip the baryonic equations of energy and state, which play no role in the structure formation dynamics, and conclude this presentation with the continuity equations:

$$\frac{d\rho_{\mathbf{bar}}}{dt} + \rho_{\mathbf{bar}}\nabla\mathbf{u}_{\mathrm{bar}} = 0 \qquad (C6)$$

$$\frac{d\rho_{\mathbf{dm}}}{dt} + \rho_{\mathbf{dm}}\nabla\mathbf{u}_{\mathrm{dm}} = 0. \qquad (C7)$$

We define $\delta\mathbf{u}_{\mathrm{bar}}$ as the baryonic peculiar velocity and $\delta\phi_{\mathrm{grav}}$ as the dark matter peculiar gravitational potential.

In addition, it is assumed that the baryonic mass fracture is much smaller than that of DM (hence the gravitational potential is given only by the DM). Under these assumptions, the linearised Euler and Continuity equations, for the baryons, in physical (Eulerian) coordinates may be written as [110]

$$\delta\dot{\mathbf{u}}_{\mathrm{bar}} = -\nabla\delta\phi_{\mathrm{grav}} - H\delta\mathbf{u}_{\mathrm{bar}} \qquad (C8)$$

$$\dot{\delta}_{\mathrm{bar}} = -\nabla \cdot \delta\mathbf{u}_{\mathrm{bar}}. \qquad (C9)$$

where $\delta \equiv \delta\rho_{\mathbf{bar}}/\bar{\rho}_{bar}$, and $\delta\rho_{\mathbf{bar}}$ is the peculiar baryonic density. From now on these equations will be developed working in comoving coordinates. To achieve this, we transform $\nabla \to \nabla/a$ and $\delta\mathbf{u}_{\mathrm{bar}} \to a\mathbf{v}_{\mathrm{bar}}$, where a is the scale factor, to get

$$\dot{\mathbf{v}}_{\mathrm{bar}} = -\nabla\phi_{\mathrm{grav}} - 2H\mathbf{v}_{\mathrm{bar}} \qquad (C10)$$

$$\dot{\delta}_{\mathrm{bar}} = -\nabla \cdot \mathbf{v}_{\mathrm{bar}} \qquad (C11)$$

where $\nabla\phi_{\mathrm{grav}}$ is given by the correspondent poison equation. In K-space $\nabla \to i\mathbf{k}$ and $\nabla^2 \to -k^2$ so in transforming these equations to K-space we have

$$\dot{\mathbf{v}}_{\mathrm{bar}} = -i\mathbf{k}\phi_{\mathrm{grav}} - 2H\mathbf{v}_{\mathrm{bar}} \qquad (C12)$$

$$\dot{\delta}_{\mathrm{bar}} = -i\mathbf{k} \cdot \mathbf{v}_{\mathrm{bar}} \qquad (C13)$$

Eq. C12 is then multiplied by $i\mathbf{k}$ and Eq. C13 is differentiated relative to t to get

$$i\mathbf{k} \cdot \dot{\mathbf{v}}_{\mathrm{bar}} = k^2\phi_{\mathrm{grav}} - i\mathbf{k}2H\mathbf{v}_{\mathrm{bar}} \qquad (C14)$$

$$\ddot{\delta}_{\mathrm{bar}} = -i\mathbf{k} \cdot \dot{\mathbf{v}}_{\mathrm{bar}} \qquad (C15)$$

taking into account Eqs. C13 and C15 we have

$$-\ddot{\delta}_{\mathrm{bar}} = k^2\phi_{\mathrm{grav}} + 2H\dot{\delta}_{\mathrm{bar}}. \qquad (C16)$$

The poison equation of gravity in comoving coordinates is

$$\phi_{\mathrm{grav}} = -\frac{4\pi G\bar{\rho}_{\mathrm{dm}}\delta_{\mathrm{dm}}}{a^3 k^2} = -\frac{3H^2\Omega_{\mathrm{m}}\delta_{\mathrm{dm}}}{2k^2} \qquad (C17)$$

with $\Omega_{\mathrm{m}} \equiv \bar{\rho}_{\mathrm{dm}}\rho_{crit}^{-1}a^{-3}$ and $\rho_{crit} \equiv 3H^2/8\pi G$. Hence, Eq. C16 can be written as

$$\ddot{\delta}_{\mathrm{bar}} + 2H\dot{\delta}_{\mathrm{bar}} = \frac{3}{2}H^2\Omega_{\mathrm{m}}\delta_{\mathrm{dm}} \qquad (C18)$$

and it is useful to define Ω_{m} in terms of it's current value Ω_{m0} as $\Omega_{\mathrm{m}} = \Omega_{\mathrm{m0}}H_0^2 H^{-2}a^{-3}$. in a similar way we can derive the linear equation for perturbations in the dark-matter density, except that this time the total potential that a DM particle feels is the gravitational potential plus the scalar potential, giving rise to a modified poison equation [1]

$$\phi_k = \phi_{\mathrm{grav}}\left(1 + \frac{\beta}{1 + (\mathbf{k}r_s)^{-2}}\right) \qquad (C19)$$

and so all in all, the perturbation equation is

$$\ddot{\delta}_{dm} + 2H\dot{\delta}_{dm} = \frac{3}{2}H^2\Omega_m C\delta_{dm} \quad \text{(C20)}$$

where

$$C \equiv 1 + \frac{\beta}{1 + (\mathbf{k}r_s)^{-2}} \quad \text{(C21)}$$

and

$$H^2 = (\frac{\dot{a}}{a})^2 \quad \text{(C22)}$$
$$= H_0^2[\Omega_{m0}(1+z)^3 + \Omega_{\Lambda 0} + \Omega_0(1+z)^2]$$

where the curvature parameter is $\Omega_0 \equiv \Omega_{m0} + \Omega_{\Lambda 0}$. Taking $z \equiv 1/a - 1$ to high numbers, one can see that $\Omega_m \to 1$ and the density fluctuations behave as in an Einstein-DeSitter universe.

for a constant r_s in an Einstein De-Sitter universe ($\Omega = 1$ and $\Omega_\Lambda = 0$) $a \propto t^{2/3}$ and $H \propto t^{-1}$ it can be checked by inspection [1] that $\delta_{dm} \propto t^p$ where

$$p = \frac{1}{6}\left(25 + \frac{24\beta}{1 + (\mathbf{k}r_s)^{-2}}\right)^{\frac{1}{2}} - \frac{1}{6} \quad \text{(C23)}$$

in contrast to the $p = 2/3$ factor when no scalar interactions are present. As for the baryonic fluctuations, $\delta_{bar} = \delta_{dm}/C$.

In this study we generalize the results of [1] for arbitrary Ω_{m0} and $\Omega_{\Lambda 0}$, while using regular scaling relations. For commodity reasons, from now on wherever we refer to $\delta(\Omega_m, C)$ if either Ω_m or C equal 1 they will be omitted. So for example, the notation of $\delta(\Omega_m = 1, C)$ becomes $\delta(C)$ and $\delta(\Omega_m = 1, C = 1)$ becomes just δ. In addition, when no species is defined for δ, it may be either one of them (either δ_{dm} or δ_{bar}).

We claim by numerical integration, that a good approximation for the solution of Eqs. C18 and C20 is

$$\frac{\delta(\Omega_m, C)}{\delta(C)} \simeq \left(\frac{\delta(\Omega_m)}{\delta}\right)^{\frac{3}{2}P} \quad \text{(C24)}$$

This can be seen in Fig. 19. The relative error of this approximation is quite small, as can be seen in the lower panel of the same figure.

for the case of $C = 1$ we have $\beta = 0$ and there are no scalar interactions - thus we may use standard approximations for the base of the RHS. for example [111]

$$\frac{\delta(\Omega_m)}{\delta} \simeq \frac{\frac{5}{2}\Omega_m}{\Omega_m^{4/7} - \Omega_\Lambda + (1 + \frac{1}{2}\Omega_m)(1 + \frac{1}{70}\Omega_\Lambda)}. \quad \text{(C25)}$$

Since $\delta(C) \propto a^{\frac{3}{2}P}$ and $\delta \propto a$ we can see from C24 that $\delta(\Omega_m, C) \propto \delta(\Omega_m)^{\frac{3}{2}P}$. And so we get an important result for velocity fields, namely

$$f \equiv \frac{d\log(\delta(\Omega_m, c))}{d\log(a)} \simeq \frac{3}{2}P\frac{d\log(\delta(\Omega_m))}{d\log(a)} \quad \text{(C26)}$$

and the derivative term of the RHS can be approximated in the usual form, for example [64]

$$\frac{d\log(\delta(\Omega_m))}{d\log(a)} \simeq \Omega_m^{0.6} \quad \text{(C27)}$$

this is almost independent of Λ, as shown in [112], which also gives a better approximation for a flat universe:

$$\frac{d\log(\delta(\Omega_m))}{d\log(a)} \simeq \Omega_m^{0.6} + \frac{1}{70}\left(1 - \frac{1}{2}\Omega_m(1 + \Omega_m)\right) \text{(C28)}$$

Next we define the baryonic velocity potential in K-space as $i\mathbf{k}\phi_v \equiv \mathbf{v}_{bar}$ so Eq. C13 is $\dot{\delta}_{bar} = k^2\phi_v$. Noting that $\dot{\delta}_{bar} = f\delta_{bar}H$ we then have

$$\frac{3}{2}Pf_1\delta_{bar}H = k^2\phi_v \quad \text{(C29)}$$

where f_1 is the normal factor f, with $C = 1$. This result is of course good also for the DM fluctuations. The velocity-density relation is thus

$$\frac{3}{2}Pf_1\delta_{bar}H = -i\mathbf{k} \cdot \mathbf{v}_{bar}. \quad \text{(C30)}$$

Linear theory is further extended by giving the baryons mass. In this case, Eq. C20 becomes

$$\ddot{\delta}_{dm} + 2H\dot{\delta}_{dm} = \frac{3}{2}H^2(\Omega_{dm}C\delta_{dm} + \Omega_{bar}\delta_{bar}). \quad \text{(C31)}$$

Lets assume that $\delta_{bar} = \delta_{dm}/f$ with constant f. Then the last equation becomes

$$\ddot{\delta}_{dm} + 2H\dot{\delta}_{dm} = \frac{3}{2}H^2\Omega_{dm}C^*\delta_{dm} \quad \text{(C32)}$$

where $C^* \equiv \Omega_{bar}/(f\Omega_{dm}) + C$. The solution to this equation was already given before. As for the baryons, Eq. C18 becomes

$$\ddot{\delta}_{bar} + 2H\dot{\delta}_{bar} = \frac{3}{2}H^2(\Omega_{bar}\delta_{bar} + \Omega_{dm}\delta_{dm}) \quad \text{(C33)}$$

Then, using the definition of f, this becomes

$$\ddot{\delta}_{dm} + 2H\dot{\delta}_{dm} = \frac{3}{2}fH^2(\Omega_{bar}\delta_{dm}/f + \Omega_{dm}\delta_{dm}) \text{ (C34)}$$
$$= \frac{3}{2}fH^2\Omega_{dm}(\Omega_{bar}/\Omega_{dm} + f)\delta_{dm} \text{ (C35)}$$

which is true if and only if it becomes Eq. C32. That means,

$$\frac{\Omega_{bar}}{f\Omega_{dm}} + C = \frac{\Omega_{dm}}{\Omega_{bar}} + f, \quad \text{(C36)}$$

which gives

$$f = \quad \text{(C37)}$$
$$\frac{C\Omega_{dm} - \Omega_{bar} + \sqrt{(C\Omega_{dm} - \Omega_{bar})^2 + 4\Omega_{dm}\Omega_{bar}}}{2\Omega_{dm}},$$

and indeed this factor is constant, since Ω_{dm} and Ω_{bar} have the same dependence on time.

This theory is compared to numerical simulations, as seen in Fig. 18, and as described in App. B. This comparison indicates on the correctness of both the simulations and the linear theory.
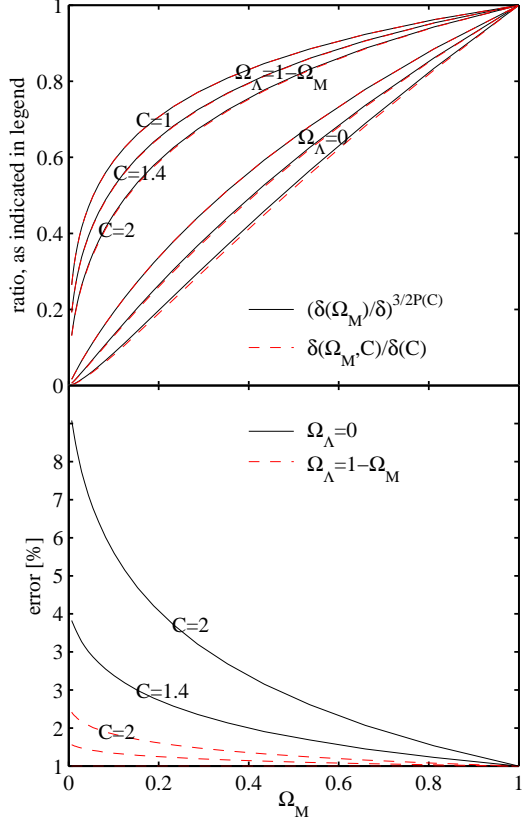
FIG. 19: Approximate analytic solution to linear theory. Upper panel compares the numerical calculation in dashed red lines, to the approximation, which corresponds to the solid blue lines. The comparison is made both for a flat universe and for an universe without dark energy, for different values of C, as indicated in the figure. The bottom panel shows the relative error in the approximation.